

A Directional Borehole Radar System

Koen W.A. van Dongen,* Ronald van Waard, and Stefan van der Baan

T&A Survey, Amsterdam, The Netherlands

Peter M. van den Berg and Jacob T. Fokkema

Centre for Technical Geoscience, Delft University of Technology, Delft,
The Netherlands

Received October 24, 2001; revised May 13, 2002

In this paper we present the simulation and design of a directional borehole radar. In addition we discuss an imaging method for the radar system. The antenna system contains an electric dipole which is in one direction shielded by a cylindrical perfectly conducting reflector. The radiation pattern of the reflected wavefield is computed by first solving the integral equation. This equation combines the unknown electric surface current density on the reflector and the known incident field from the electric dipole. Once the electric surface current density is known, the radiation pattern of the system is computed using the integral representation over the reflector and the dipole. The radiation patterns for various configurations have been computed in order to find an optimal configuration. A prototype of the antenna system based on an optimal configuration has been built, and the directional radiation pattern has been measured in the plane perpendicular to the antenna system. The measurements were in good agreement with the computations. Subsequently a three dimensional imaging method for the borehole radar is presented. Here a deconvolution is carried out in the angular direction, making use of the computed radiation pattern. Some imaging results will be shown.

Key Words. GPR, directional borehole radar, imaging.

1. Introduction

There are many situations all over the world where one would like to know how the subsurface is built up. Electromagnetic measurements with ground penetrating radar (GPR) from the surface might give an answer,

*To whom all correspondence should be addressed. Post: P.O. Box 5031, 2600 GA Delft, The Netherlands; e-mail: K.W.A.VanDongen@its.tudelft.nl

but problems arise if the volume of interest is unreachable for such methods. For example, in the oil and gas industry where the oil containing sand layer of interest, especially the top and the bottom of an oil reservoir, is simply too deep. In such case GPR measurements in a borehole is then a good solution as long as the system is directional. Unfortunately, with these systems directionality is often offset against penetration. The radar system we present fits in a single borehole. In addition it combines directionality and large penetration by focusing the emitted energy. The system has in both radial and angular direction a good resolution. First we discuss the modeling and design of the antenna system which consists of an electric dipole and a curved reflector. The radiation pattern of the antenna system is computed by first solving the integral equation for the unknown electric surface current density on the reflector. This is done via a FFT Conjugate Gradient method. Next the total electric wavefield is computed using the integral representation over the dipole and the reflector. Finally we discuss an imaging method to obtain a three-dimensional image of the subsurface. Here a one step deconvolution of the measured data for the computed radiation pattern is carried out. Imaging results based on both synthetic data and measured data will be shown.

2. Antenna Design

The antenna system contains an electric dipole which is partly shielded by a curved reflector. In order to compute the effect of the reflector on the omni-directional radiation pattern of the electric dipole antenna, an integral equation is derived. This equation relates the known incident electric wavefield from the electric dipole antenna with the unknown electric surface current density at the reflector. Once the discretized integral equation is solved, via a FFT Conjugate Gradient method, the electric wavefield from the dipole shielded with the reflector is computed. A numerical example will show the focusing effect of the reflector and some experimental results are used to verify our numerical results.

2.1. Antenna Configuration

A position in the Cartesian coordinate system is denoted by the vector $\mathbf{x} = x_i = (x, y, z)$ whereas the same position is described in the orthogonal circular cylindrical coordinate system by the vector $\mathbf{v} = v_i = \{x, r, \phi\}$. The correspondence between both vectors is given by

$$\{x, y, z\} = \{x, r \cos(\phi), r \sin(\phi)\}, \quad (1)$$

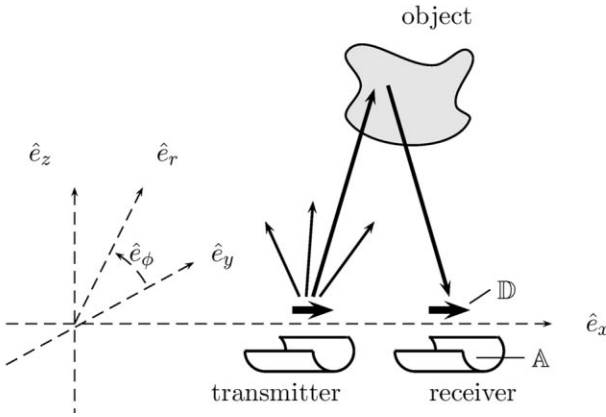


Figure 1. The bistatic antenna configuration and the two coordinate systems: the Cartesian with unit vectors $\{\hat{e}_x, \hat{e}_y, \hat{e}_z\}$ and the cylindrical with unit vectors $\{\hat{e}_r, \hat{e}_\phi, \hat{e}_z\}$.

see Figure 1. Consequently the coordinate transformation matrices T_{ij} and T_{ij}^{-1} are defined via

$$u_{x_i}(\mathbf{v}) = T_{ij} u_{v_j}(\mathbf{v}), \quad u_{v_i}(\mathbf{v}) = T_{ij}^{-1} u_{x_j}(\mathbf{v}), \quad (2)$$

where $u_{x_i}(\mathbf{v})$ and $u_{v_i}(\mathbf{v})$ are both positioned in the cylindrical coordinate system at \mathbf{v} , defined in the Cartesian and cylindrical coordinate system and pointing in the direction x_i and v_i respectively. Note that we use Einstein's summation convention for repeated subscripts.

The dipole is defined in the cylindrical coordinate system in the spatial domain \mathbb{D} ,

$$\mathbb{D} = \{v_i \in \mathbb{R}^3 \mid -d_1 < x < d_1, r = d_2, \phi = d_3\}. \quad (3)$$

Next to the dipole, a perfectly conducting rectangular circular cylindrical curved plate acts as a reflector. The area \mathbb{A} of this reflector is defined in the cylindrical coordinate system as

$$\mathbb{A} = \{v_i \in \mathbb{R}^3 \mid -a_1 < x < a_1, r = a_2, -a_3 < \phi < a_3\}. \quad (4)$$

The configuration is embedded in a homogeneous medium with constant electric permittivity ϵ , vacuum magnetic permeability μ_0 and electric conductivity σ . Here permittivity ϵ equals

$$\epsilon = \epsilon_0 \epsilon_r, \quad (5)$$

where ϵ_0 equals the permittivity of vacuum and ϵ_r the relative permittivity of the medium.

Our analysis is carried out in the temporal Laplace domain, with Laplace parameter $s = -i\omega$, where ω equals $2\pi f$ with f the frequency. We use the symbol $\hat{\cdot}$ to indicate that the specified quantity is in this temporal Laplace domain.

2.2. Formulation of the Integral Equation

The electric part of the wavefield generated by the dipole, in absence of the reflector, is denoted as $\hat{E}_{x_i}^{\text{dip}}(\mathbf{x})$. The total field in presence of the reflector is given by $\hat{E}_{x_i}^{\text{tot}}(\mathbf{x})$. Then, the scattered field due to the presence of the reflector, is defined as $\hat{E}_{x_i}^{\text{sct}}(\mathbf{x})$,

$$\hat{E}_{x_i}^{\text{sct}}(\mathbf{x}) = \hat{E}_{x_i}^{\text{tot}}(\mathbf{x}) - \hat{E}_{x_i}^{\text{dip}}(\mathbf{x}), \quad \forall \mathbf{x} \in \mathbb{R}^3. \quad (6)$$

The wavefield from an electric dipole in a Cartesian coordinate system can be derived from Maxwell equations and equals

$$\begin{aligned} \hat{E}_{x_i}^{\text{dip}}(\mathbf{x}) &= \frac{1}{s\mathcal{E}} (-\hat{\gamma}^2 \delta_{ij} + \nabla_{x_i} \nabla_{x_j} \cdot) \int_{x' \in \mathbb{D}} \hat{G}(\mathbf{x}|\mathbf{x}') \hat{J}_{x_j}^{\text{dip}}(\mathbf{x}') dA(\mathbf{x}') \\ &= \frac{1}{s\mathcal{E}} (-\hat{\gamma}^2 \delta_{ij} + \nabla_{x_i} \nabla_{x_j} \cdot) \hat{A}_{x_j}^{\text{dip}}(\mathbf{x}), \end{aligned} \quad (7)$$

with

$$\hat{\gamma}^2 = s^2 \left(\mathcal{E} + \frac{\sigma}{s} \right) \mu_0, \quad (8)$$

δ_{ij} the Kronecker delta tensor, $\nabla_{x_i} \nabla_{x_j} \cdot$ the gradient divergence operator, $\hat{G}(\mathbf{x}|\mathbf{x}')$ the Green's function of the medium, $\hat{A}_{x_j}^{\text{dip}}(\mathbf{x})$ the electric vector potential and where $\hat{J}_{x_j}^{\text{dip}}(\mathbf{x}')$ is obtained from a unit time domain delta pulse electric surface current density at the dipole. Using the coordinate transformation matrices defined in Eq. (2), Eq. (7) is formulated in a cylindrical coordinate system as

$$\hat{E}_{v_i}^{\text{dip}}(\mathbf{v}) = \frac{1}{s\mathcal{E}} (-\hat{\gamma}^2 \delta_{ij} + \nabla_{v_i} \nabla_{v_j} \cdot) \hat{A}_{v_j}^{\text{dip}}(\mathbf{v}), \quad (9)$$

with

$$\hat{A}_{v_j}^{\text{dip}}(\mathbf{v}) = \mathbf{T}_{jk} \int_{v' \in \mathbb{D}} \hat{G}(\mathbf{v}|\mathbf{v}') \mathbf{T}_{kl}^{-1} \hat{J}_{v_l}^{\text{dip}}(\mathbf{v}') dA(\mathbf{v}'). \quad (10)$$

The scattered wavefield is caused by an electric surface current density at the surface of the reflector, due to the presence of the incident electric wavefield, and is given by

$$\hat{E}_{v_i}^{\text{sct}}(\mathbf{v}) = \frac{1}{s\mathcal{E}} (-\hat{\gamma}^2 \delta_{\alpha j} + \nabla_{v_i} \nabla_{v_j} \cdot) \hat{A}_{v_j}^{\text{sct}}(\mathbf{v}), \quad (11)$$

with

$$\hat{A}_{v_j}^{\text{sct}}(\mathbf{v}) = \mathbb{T}_{jk} \int_{\mathbf{v}' \in \mathbb{A}} \hat{G}(\mathbf{v}|\mathbf{v}') \mathbb{T}_{kl}^{-1} \hat{J}_{v_l}^{\text{rfl}}(\mathbf{v}') dA(\mathbf{v}'), \quad (12)$$

where $\hat{J}_{v_m}^{\text{rfl}}(\mathbf{v}') = \{\hat{J}_x^{\text{rfl}}(\mathbf{v}'), 0, \hat{J}_\phi^{\text{rfl}}(\mathbf{v}')\}$ are the two unknown surface current densities at the reflector. At this surface, electromagnetic boundary conditions require that components of the total electric field, $\hat{E}_{v_i}^{\text{tot}}(\mathbf{v})$, tangential to this surface vanish and therefore

$$\hat{E}_{v_\alpha}^{\text{sct}}(\mathbf{v}) = -\hat{E}_{v_\alpha}^{\text{dip}}(\mathbf{v}), \quad \forall \mathbf{v} \in \mathbb{A}, \quad \forall \alpha \in \{1, 3\}, \quad (13)$$

where we use Greek subscripts α and β to denote the tangential character of the quantity. Taking the point of observation on the reflector, we end up with the following integral equation

$$-\hat{E}_{v_\alpha}^{\text{dip}}(\mathbf{v}) = \frac{1}{s\mathcal{E}} (-\hat{\gamma}^2 \delta_{\alpha j} + \nabla_{v_\alpha} \nabla_{v_j} \cdot) \hat{A}_{v_j}^{\text{sct}}(\mathbf{v}) \quad (14)$$

where the vector potential $\hat{A}_{v_j}^{\text{sct}}(\mathbf{v})$ is defined in (12).

2.3. Solution of the Integral Equation

Combining Eqs. (14) and (12) we write the integral equation as

$$-\hat{E}_{v_\alpha}^{\text{dip}}(\mathbf{v}) = \frac{1}{s\mathcal{E}} (-\hat{\gamma}^2 \delta_{\alpha j} + \nabla_{v_\alpha} \nabla_{v_j} \cdot) \mathbb{T}_{jk} \int_{\mathbf{v}' \in \mathbb{A}} \hat{G}(\mathbf{v}|\mathbf{v}') \tilde{\mathbb{T}}_{k\beta} \hat{J}_{v_\beta}^{\text{rfl}}(\mathbf{v}') dA(\mathbf{v}') \quad (15)$$

in which we have defined the following known and unknown quantities

$$\hat{J}_{v_\beta}^{\text{rfl}}(\mathbf{v}) = \begin{pmatrix} \hat{J}_x^{\text{rfl}}(\mathbf{v}) \\ \hat{J}_\phi^{\text{rfl}}(\mathbf{v}) \end{pmatrix}, \quad \hat{E}_{v_\alpha}^{\text{dip}}(\mathbf{v}) = \begin{pmatrix} \hat{E}_x^{\text{dip}}(\mathbf{v}) \\ \hat{E}_\phi^{\text{dip}}(\mathbf{v}) \end{pmatrix} \quad (16)$$

the matrices

$$\tilde{\mathbb{T}}_{k\beta} = \begin{pmatrix} 1 & 0 \\ 0 & -\sin(\phi) \\ 0 & \cos(\phi) \end{pmatrix}, \quad \mathbb{T}_{jk} = \begin{pmatrix} 1 & 0 & 0 \\ 0 & \cos(\phi) & \sin(\phi) \\ 0 & -\sin(\phi) & \cos(\phi) \end{pmatrix}, \quad \delta_{\alpha j} = \begin{pmatrix} 1 & 0 & 0 \\ 0 & 0 & 1 \end{pmatrix}, \quad (17)$$

and the gradient divergence operator

$$\nabla_{v_\alpha} \nabla_{v_j} \cdot = \begin{pmatrix} \partial_x^2 & \frac{1}{r} \partial_x \partial_r & \frac{1}{r} \partial_x \partial_\phi \\ \frac{1}{r} \partial_\phi \partial_x & \frac{1}{r^2} \partial_\phi \partial_r & \frac{1}{r^2} \partial_\phi^2 \end{pmatrix}. \quad (18)$$

Note that the $\tilde{\mathbb{T}}$ is a reduced form of \mathbb{T}^{-1} , the inverse of \mathbb{T} . Equation (15) is solved numerically using a discretization procedure as suggested by Zwamborn and Van den Berg [1]. Therefore we approximate the differential operator of Eq. (18) by a finite difference operator [2]. Furthermore the plate domain is discretized into subdomains \mathbb{A}_{mn} as shown in Figure 2, viz.

$$\mathbb{A}_{mn} = \{\mathbf{v} \in \mathbb{R}^3 \mid x_{m-1} < x < x_m, r = a_2, \phi_{n-1} < \phi < \phi_n\}, \tag{19}$$

for

$$x_m = m\Delta x, \quad \text{for } m = -M, \dots, M, \tag{20}$$

$$\phi_n = n\Delta\phi, \quad \text{for } n = -N, \dots, N. \tag{21}$$

The quantities $\hat{E}_{v_\alpha}^{\text{dip}}(\mathbf{v})$ and $\hat{J}_{v_\alpha}^{\text{rfl}}(\mathbf{v})$ are defined on a staggered grid as shown in Figure 2,

$$\hat{E}_{v_\alpha}^{\text{dip}}(\mathbf{v}) = \begin{pmatrix} \hat{E}_{x_{mn}}^{\text{dip}} \\ \hat{E}_{\phi_{mn}}^{\text{dip}} \end{pmatrix} = \begin{pmatrix} \hat{E}_x^{\text{dip}}(m\Delta x, a_2, (n - \frac{1}{2})\Delta\phi) \\ \hat{E}_\phi^{\text{dip}}((m - \frac{1}{2})\Delta x, a_2, n\Delta\phi) \end{pmatrix} \tag{22}$$

for $m = -M, \dots, M$ and $n = -N, \dots, N$,

$$\hat{J}_{v_\beta}^{\text{rfl}}(\mathbf{v}) = \begin{pmatrix} \hat{J}_{x_{mn}}^{\text{rfl}} \\ \hat{J}_{\phi_{mn}}^{\text{rfl}} \end{pmatrix} = \begin{pmatrix} \hat{J}_x^{\text{rfl}}(m\Delta x, a_2, (n - \frac{1}{2})\Delta\phi) \\ \hat{J}_\phi^{\text{rfl}}((m - \frac{1}{2})\Delta x, a_2, n\Delta\phi) \end{pmatrix} \tag{23}$$

for $m = -M, \dots, M$ and $n = -N, \dots, N$.

The consequently obtained discretized integral equation is solved using a FFT Conjugate Gradient method as in [1]. Therefore we replace our integral equation by an operator equation, viz.

$$\mathbf{f}_{v_\alpha} = (\mathbb{L}j)_{v_\alpha}, \tag{24}$$

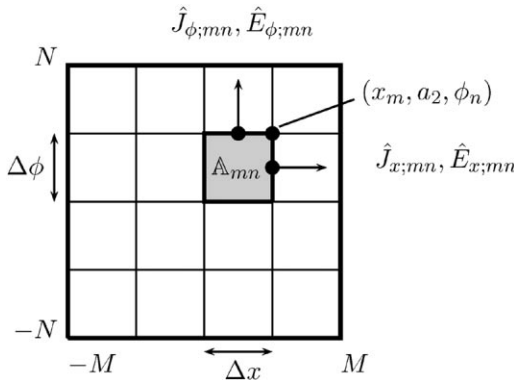


Figure 2. The discretization of the plate domain \mathbb{A} into subdomains \mathbb{A}_{mn} .

where \mathbf{f}_{v_α} is obtained from the known incident wavefield, and $(\mathbf{L}j)_{v_\alpha}$ the operation \mathbf{L} applied on the electric surface current density j on the reflector. Furthermore, we define the L_2 norm via the inner product of two vectorial quantities in the spatial domain \mathbb{A} , viz.

$$\begin{aligned} \|\mathbf{u}_{v_\alpha}\|_{\mathbb{A}}^2 &= \langle \mathbf{u}_{v_\alpha}, \bar{\mathbf{u}}_{v_\alpha} \rangle_{\mathbb{A}} \\ &= \sum_{m=-M+1}^{M-1} \sum_{n=-N+1}^N \mathbf{u}_{x;mn} \bar{\mathbf{u}}_{x;mn} a_2 \Delta x \Delta \phi \\ &\quad + \sum_{m=-M+1}^M \sum_{n=-N+1}^{N-1} \mathbf{u}_{\phi;mn} \bar{\mathbf{u}}_{\phi;mn} a_2 \Delta x \Delta \phi, \end{aligned} \tag{25}$$

in which the overbar denotes the complex conjugate. To quantify the residual $\mathbf{f}_{v_\alpha} - (\mathbf{L}j)_{v_\alpha}$ for Eq. (24) we define the error norm

$$r_{v_\alpha} = \|\mathbf{f}_{v_\alpha} - (\mathbf{L}j)_{v_\alpha}\|_{\mathbb{A}}. \tag{26}$$

Finally, the normalized error function ERR which is minimized is defined as

$$ERR = \frac{\|r_{v_\alpha}\|_{\mathbb{A}}}{\|\hat{\mathbf{E}}_{v_\alpha}^{\text{dip}}\|_{\mathbb{A}}}. \tag{27}$$

2.4. Numerical and Experimental Results

Simulations are carried out to design an optimal configuration. The dipole is positioned at a radial distance of approximately 0.05 m. The reflector is positioned at the same radial distance and curved over approximately 150° and we use 26 cells in the x -direction and 16 cells in the ϕ -direction. The system is embedded in a non-conducting medium, $\sigma = 0$, with relative permittivity $\epsilon_r = 80$. Computations are carried out for the 100 MHz components of the electromagnetic wavefields and the iterative process is stopped when the normalized error satisfies $ERR \leq 0.01$. In Figure 3 we present the normalized error as a function of the number of iterations. The results for the electric surface current densities are shown in Figure 4. From this figure we observe that the components of the current densities normal to the edges vanish, as we expect. The components tangential to the edges tend to large values. Theoretically, they should grow to infinity if the element size was taken infinitely small. This is avoided since a finite element size is taken, and the average value over this element is computed.

Using these surface currents, we compute the scattered and total electric wavefields. In Figures 5(a) and 5(b) the total electric wavefield in the plane $x = 0$ and $y = 0$ are shown. Clearly visible is the effect of the presence of the reflector on the radiation pattern of a dipole. However, the aim is

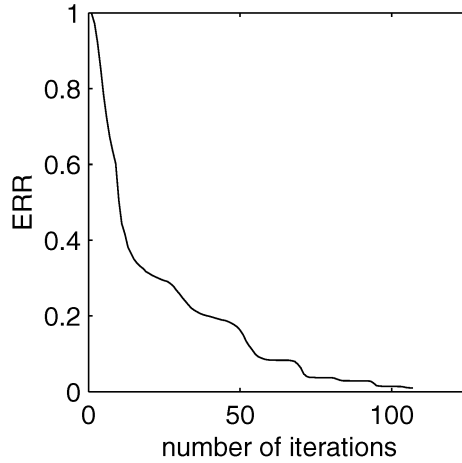


Figure 3. The normalized error ERR as a function of the number of iterations.

not only to disturb the omni-directional radiation pattern of an electric dipole but also to increase penetration into the subsurface by focusing the wavefield. Therefore it is interesting to compute the gain factor $|E^{\text{tot}}|/|E^{\text{dip}}|$, as shown in Figures 6(a) and 6(b).

Based on this design a prototype antenna system is built for experimental verification of the antenna model. The radiation pattern of this prototype

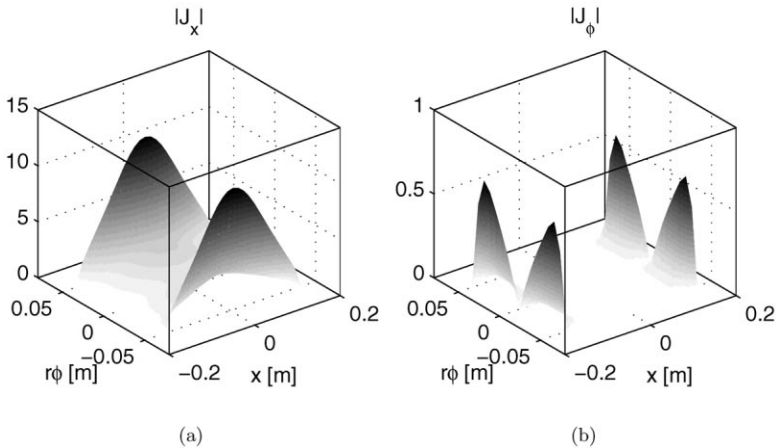


Figure 4. The electric surface current density at the surface of the reflector: (a) the absolute value of J_x and (b) the absolute value of J_ϕ .

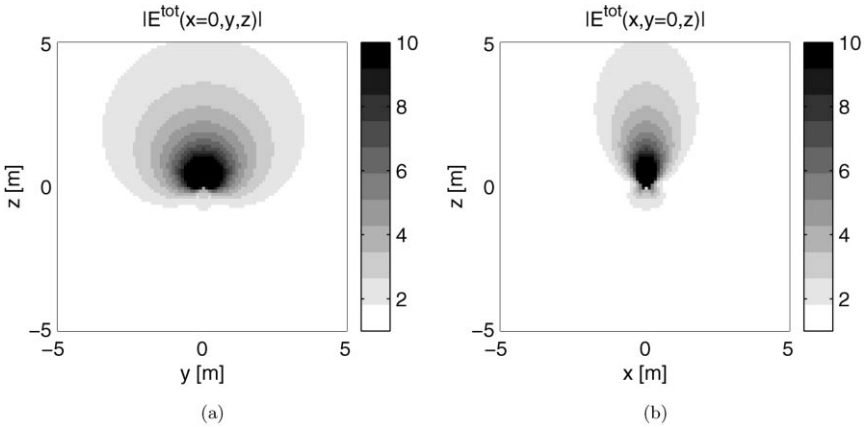


Figure 5. The computed total electric wavefield in the plane (a) $x = 0$ and (b) $y = 0$.

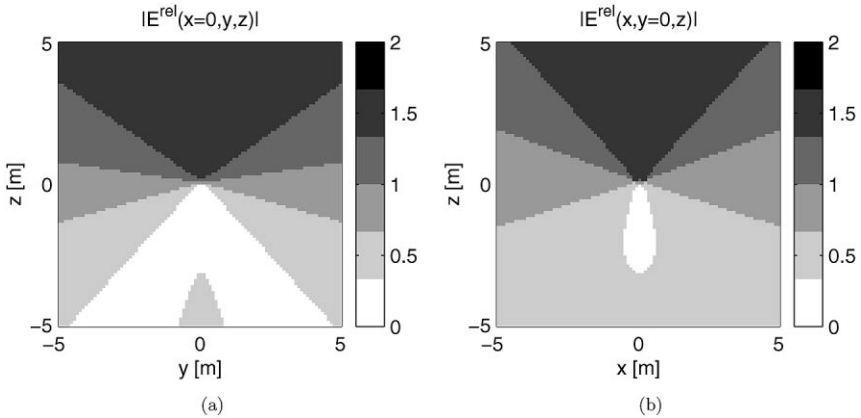


Figure 6. The normalized electric wavefield, $|E^{rel}(\mathbf{x})| = |E^{tot}(\mathbf{x})|/|E^{dip}(\mathbf{x})|$, in the plane (a) $x = 0$ and (b) $y = 0$.

is measured at a radial distance of $r = 0.3$ m in the plane $x = 0$. In Figure 7 the measured and computed radiation patterns are shown. Both curves are normalized by putting their maximum values to unity. We observe an excellent agreement between both curves.

3. Imaging Based on Back Propagation

The imaging algorithm described in this section is based on a deconvolution of the measured data for the previously computed radiation pattern

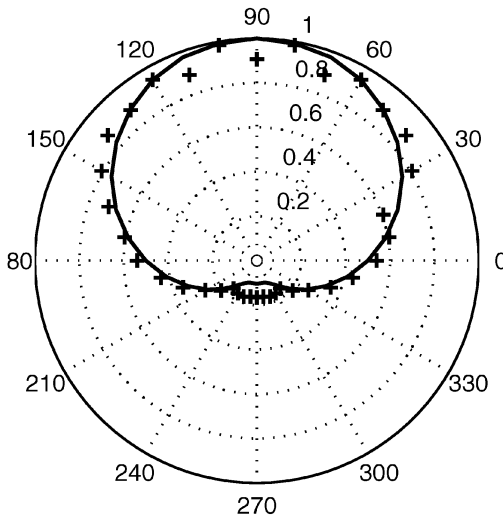


Figure 7. The computed (solid line) and measured (crosses) normalized radiation pattern.

of the antenna system. Starting with the reciprocity theorem an integral equation is derived which describes the change of impedance of the antenna system as a function of the change in contrast in the background medium. An approximate solution of this integral equation, and consequently a 3D image of the subsurface, is obtained via a one step inversion procedure, the so called back propagation.

3.1. Change of Antenna Impedance Due to Anomalies in the Background Medium

The reciprocity theorem [3] is used to correlate two field states occurring in the same spatial domain \mathbb{D} . In Figure 8, the two states A and B are shown as described in Table 1. In state A, the closed surface $\partial\mathbb{D}$ with normal \mathbf{v}_i encloses the source free spatial domain \mathbb{D} which is a homogeneous background medium that is, in addition, linear, time-invariant, instantaneously reacting, locally reacting, and isotropic in its electromagnetic behavior. The medium is described by the parameters $\hat{\eta}^{\text{bg}}(\mathbf{x})$,

$$\hat{\eta}^{\text{bg}}(\mathbf{x}) = \sigma^{\text{bg}}(\mathbf{x}) + s\mathcal{E}^{\text{bg}}(\mathbf{x}), \quad (28)$$

and $\hat{\zeta}$,

$$\hat{\zeta} = s\mu_0. \quad (29)$$

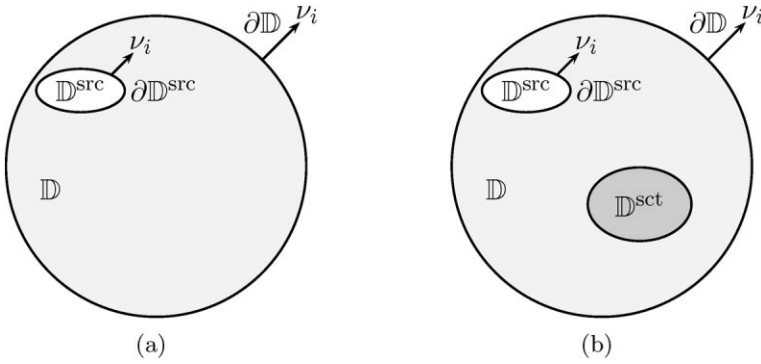


Figure 8. Two states of the same spatial domain \mathbb{D} with boundary $\partial\mathbb{D}$ and with inaccessible volume action antenna source domain $\mathbb{D}^{\text{src}} \not\subset \mathbb{D}$. The source domain contains a receiving and transmitting antenna. In state A (a) the electromagnetic properties are $\hat{\eta}^A(\mathbf{x}) = \hat{\eta}(\mathbf{x})$ and $\hat{\zeta}^A = \hat{\zeta}$, and state B (b) has the same background medium and a scattering domain $\mathbb{D}^{\text{sct}} \subset \mathbb{D}$, with $\hat{\eta}^B(\mathbf{x}) = \hat{\eta}^{\text{sct}}(\mathbf{x})$ and $\hat{\zeta}^B = \hat{\zeta}$.

The domain encloses an inaccessible volume action antenna source domain $\mathbb{D}^{\text{src}} \not\subset \mathbb{D}$ which contains the transmitting and receiving antennas. The only fields present are the electromagnetic background wavefields. In state B, we have the same spatial domain \mathbb{D} and the same medium parameters where in this case the boundary $\partial\mathbb{D}$ also encloses a domain \mathbb{D}^{sct} , due to the presence of an object with medium parameters $\hat{\eta}^{\text{sct}}(\mathbf{x})$ and $\hat{\zeta}$.

For these two states the reciprocity theorem is written as

$$\begin{aligned}
 & \mathcal{E}_{m,r,p} \int_{x \in \partial\mathbb{D}} \mathbf{v}_m [\hat{E}_r^A(\mathbf{x}) \hat{H}_p^B(\mathbf{x}) - \hat{E}_r^B(\mathbf{x}) \hat{H}_p^A(\mathbf{x})] dA \\
 & \quad - \mathcal{E}_{m,r,p} \int_{x \in \partial\mathbb{D}^{\text{src}}} \mathbf{v}_m [\hat{E}_r^A(\mathbf{x}) \hat{H}_p^B(\mathbf{x}) - \hat{E}_r^B(\mathbf{x}) \hat{H}_p^A(\mathbf{x})] dA \\
 & = \int_{x \in \mathbb{D}} -[\eta_{r,k}^B(\mathbf{x}) - \eta_{k,r}^A(\mathbf{x})] \hat{E}_r^A(\mathbf{x}) \hat{E}_k^B(\mathbf{x}) dV. \tag{30}
 \end{aligned}$$

Table 1. Description of the States A and B for the Spatial Domain \mathbb{D}

| state A | state B |
|-----------------------------------------------------------------------------------|---------------------------------------------------------------------------------------------------------------------------------------------------------------------------------------------------------------|
| $\{\hat{E}_p^A, \hat{H}_q^A\} = \{\hat{E}_p^{\text{bg}}, \hat{H}_q^{\text{bg}}\}$ | $\{\hat{E}_p^B, \hat{H}_q^B\} = \{\hat{E}_p^{\text{tot}}, \hat{H}_q^{\text{tot}}\} = \{\hat{E}_p^{\text{bg}} + \hat{E}_p^{\text{sct}}, \hat{H}_q^{\text{bg}} + \hat{H}_q^{\text{sct}}\}$ |
| $\{\hat{\eta}^A, \hat{\zeta}^A\} = \{\hat{\eta}^{\text{bg}}, \hat{\zeta}\}$ | $\{\hat{\eta}^B, \hat{\zeta}^B\} = \{(\hat{\eta}^{\text{sct}}, \hat{\zeta}), (\hat{\eta}^{\text{bg}}, \hat{\zeta})\} \{ \mathbf{x} \in \mathbb{D}^{\text{sct}}, \mathbf{x} \notin \mathbb{D}^{\text{sct}} \}$ |
| $\{\hat{J}_p^A, \hat{K}_q^A\} = \{0, 0\}$ | $\{\hat{J}_p^B, \hat{K}_q^B\} = \{0, 0\}$ |

The first integral over the outer boundary vanishes, since in both states the medium parameters outside $\partial\mathbb{D}$ are the same, and since there are no sources outside $\partial\mathbb{D}$. The boundary integral over the source domain can be approximated as follows by putting, in the low frequency range,

$$\hat{E}_i(\mathbf{x}) = -\partial_i \hat{\phi}(\mathbf{x}), \quad (31)$$

where $\hat{\phi}$ is the electric potential. Using Stokes' theorem the integral over the boundary of the source domain is obtained as

$$\begin{aligned} \varepsilon_{m,r,p} \int_{\mathbf{x} \in \partial\mathbb{D}^{\text{src}}} v_m [\hat{E}_r^A(\mathbf{x}) \hat{H}_p^B(\mathbf{x}) - \hat{E}_r^B(\mathbf{x}) \hat{H}_p^A(\mathbf{x})] dA \\ = \int_{\mathbf{x} \in \partial\mathbb{D}^{\text{src}}} v_m [\hat{\phi}^A(\mathbf{x}) \hat{\eta}^B(\mathbf{x}) \hat{E}_m^B(\mathbf{x}) - \hat{\phi}^B(\mathbf{x}) \hat{\eta}^A(\mathbf{x}) \hat{E}_m^A(\mathbf{x})] dA. \end{aligned} \quad (32)$$

The antennas in the source domain are described as perfect conductors which form an N-ports system, where each termination port has a surface \mathbb{A}_α , for $\alpha = 1, \dots, N$. Since the electric potential $\hat{\phi}^{A,B}(\mathbf{x})$ is constant over such a termination port, each terminal α has a constant potential \hat{V}_α . At each port the Maxwell current density $\hat{J}_k(\mathbf{x}) + s\hat{D}_k(\mathbf{x})$ is dominated by the electric current density $\hat{J}_k(\mathbf{x})$ in the low frequency approximation and consequently the electric line current density I_α is used. So from the constitutive relations in combination with the electromagnetic boundary conditions the right-hand side of Eq. (32) is written as a finite summation over the terminals, i.e.,

$$\begin{aligned} \int_{\mathbf{x} \in \partial\mathbb{D}^{\text{src}}} v_m [\hat{\phi}^A(\mathbf{x}) \hat{\eta}^B(\mathbf{x}) \hat{E}_m^B(\mathbf{x}) - \hat{\phi}^B(\mathbf{x}) \hat{\eta}^A(\mathbf{x}) \hat{E}_m^A(\mathbf{x})] dA \\ = \sum_{\alpha=1}^N \int_{\mathbf{x} \in \mathbb{A}_\alpha} v_m [\hat{\phi}^A(\mathbf{x}) \hat{J}_m^B(\mathbf{x}) - \hat{\phi}^B(\mathbf{x}) \hat{J}_m^A(\mathbf{x})] dA \\ = \sum_{\alpha=1}^N [\hat{V}_\alpha^A \hat{I}_\alpha^B - \hat{V}_\alpha^B \hat{I}_\alpha^A]. \end{aligned} \quad (33)$$

The electric potentials and line current densities in the antennas are coupled via the impedance matrix $\hat{Z}_{\alpha\beta}$ as

$$\hat{V}_\alpha = \hat{Z}_{\alpha\beta} \hat{I}_\beta \quad \text{for } \{\alpha, \beta\} = 1, \dots, N. \quad (34)$$

Combining Eqs. (30), (32), and (33) with the state descriptions as formulated in Table 1 results in

$$\delta \hat{Z}_{\alpha\beta} \hat{I}_\alpha^A \hat{I}_\beta^B = - \int_{\mathbf{x} \in \mathbb{D}} [\eta^B(\mathbf{x}) - \eta^A(\mathbf{x})] \hat{E}_k^A(\mathbf{x}) \hat{E}_k^B(\mathbf{x}) dV, \quad (35)$$

where $\delta\hat{Z}_{\alpha\beta}$ is the difference in impedance between two states,

$$\delta\hat{Z}_{\alpha\beta} = \hat{Z}_{\alpha\beta}^A - \hat{Z}_{\alpha\beta}^B. \quad (36)$$

The electric field strength is linearly dependent on the electric line current density $\hat{I}_\alpha^{A,B}$, so

$$\hat{E}_k^{A,B}(\mathbf{x}) = \hat{e}_{\alpha;k}^{A,B}(\mathbf{x})\hat{I}_\alpha^{A,B} \quad (37)$$

in which $\hat{e}_{\alpha;k}^A = \hat{e}_{\alpha;k}^{\text{bg}}$ and $\hat{e}_{\alpha;k}^B = \hat{e}_{\alpha;k}^{\text{tot}}$ are the electric field strengths caused by their unit current densities. Substitution of Eq. (37) in Eq. (35) gives an integral equation describing the change of impedance, $\delta\hat{Z}_{\alpha\beta}$, due to an anomaly $\delta\hat{\eta}(\mathbf{x}) = \hat{\eta}^{\text{bg}}(\mathbf{x}) - \hat{\eta}^{\text{sci}}(\mathbf{x})$ in the background medium, viz.,

$$\delta\hat{Z}_{\alpha\beta} = \int_{\mathbf{x} \in \mathbb{D}} \delta\hat{\eta}(\mathbf{x})\hat{e}_{\alpha;k}^{\text{bg}}(\mathbf{x})\hat{e}_{\beta;k}^{\text{tot}}(\mathbf{x}) dV. \quad (38)$$

This integral equation will serve as a starting point for the imaging algorithm.

3.2. Measuring in Bistatic Mode

Based on the design presented in Section 2 of this chapter a bistatic antenna system has been built. Applying Eq. (34) to this setup, ($N = 2$), we obtain the following equation

$$\hat{V}_2 = \hat{Z}_{21}\hat{I}_1 + \hat{Z}_{22}\hat{I}_2, \quad (39)$$

where \hat{V}_2 represents the voltage measured at the receiver, \hat{I}_1 the electric source current at the transmitter, \hat{Z}_{21} the mutual impedance of the transmitter and the receiver and \hat{Z}_{22} the self impedance of the receiver. Note that we assume the medium to be reciprocal and consequently $\hat{Z}_{12} = \hat{Z}_{21}$. Since the receiver voltage is measured over an open end port, the current through the receiver equals zero, $\hat{I}_2 = 0$. Therefore the measured voltage at the receiver, \hat{V}_2 , in Eq. (39) equals

$$\hat{V}_2^{\text{rec}} = \hat{Z}_{12}\hat{I}_1^{\text{trans}} \quad (40)$$

since $\hat{V}_2 = \hat{V}_2^{\text{rec}}$ and $\hat{I}_1 = \hat{I}_1^{\text{trans}}$.

In Figure 9 it is shown how in a bistatic setup measurements take place at “discrete” positions $\mathbf{v}^{(k)}$ for the system, viz.

$$\mathbf{v}^{(k)} = (x^{(k)}, 0, \phi^{(k)}) \quad (41)$$

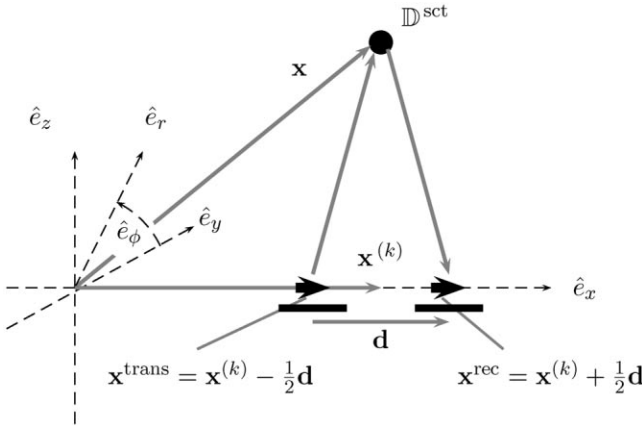


Figure 9. The setup in bistatic mode.

Adapting integral equation (38) for these discrete positions and combining it with the results shown in Eq. (40), we obtain the following integral equation

$$\frac{\delta \hat{V}^{\text{rec}}(\mathbf{v}^{(k)})}{\hat{I}^{\text{trans}}} = \int_{\mathbf{v} \in \mathbb{D}} \delta \eta(\mathbf{v}) \hat{S}(\mathbf{v} | \mathbf{v}^{(k)}) dV. \quad (42)$$

in which the sensitivity function $\hat{S}(\mathbf{v} | \mathbf{v}^{(k)})$ describes the combination of the transmitter and receiver patterns of the antenna system,

$$\begin{aligned} \hat{S}(\mathbf{v} | \mathbf{v}^{(k)}) &= \hat{S}(x - x^{(k)}, r, \phi - \phi^{(k)}) \\ &= \hat{e}_j^{\text{trans}; \text{bg}}\left(x - x^{(k)} + \frac{1}{2}d, r, \phi - \phi^{(k)}\right) \hat{e}_j^{\text{rec}; \text{bg}}\left(x - x^{(k)} - \frac{1}{2}d, r, \phi - \phi^{(k)}\right), \end{aligned} \quad (43)$$

where $\hat{e}_j^{\text{trans}; \text{bg}}(\mathbf{v})$ and $\hat{e}_j^{\text{rec}; \text{bg}}(\sigma)$ are the electric wavefields in the background medium produced by an electric unit current at the transmitter and the receiver position, respectively. These radiation patterns are approximately equal to the patterns computed at the central frequency of 100 MHz. Note that the Born approximation is used to approximate $\hat{e}_j^{\text{rec}; \text{tot}}(\mathbf{v})$ by $\hat{e}_j^{\text{rec}; \text{bg}}(\mathbf{v})$. Besides, we assume the contrast to be frequency independent, $\delta \hat{\eta}(\mathbf{v}) = \delta \eta(\mathbf{v})$.

In view of the presence of convolution and periodicity in the angular direction, we take advantage of the properties of discrete Fourier series. This series is defined as

$$f(\phi) = \sum_{n=-\infty}^{\infty} f^{(n)} e^{in\phi}, \quad (44)$$

where

$$f^{(n)} = \frac{1}{2\pi} \int_{\phi=0}^{2\pi} f(\phi) e^{-in\phi} d\phi. \quad (45)$$

Applying these discrete Fourier transforms to Eq. (42) leads to decoupled equations in the discrete angular Fourier domain

$$\frac{\delta \hat{V}^{(n); \text{rec}}(x^{(k)})}{\hat{I}^{\text{trans}}} = \int_{x=-\infty}^{\infty} \int_{r=0}^{\infty} \delta \eta^{(n)}(x, r) \hat{S}^{(n)}(x - x^{(k)}, r) r dr dx, \quad \forall n = -\infty, \dots, \infty, \quad (46)$$

where

$$\hat{S}^{(n)}(x, r) = \frac{1}{2\pi} \int_{\phi=0}^{2\pi} e^{-in\phi} \hat{S}(x, r, \phi) d\phi, \quad (47)$$

$$\delta \hat{V}^{(n); \text{rec}}(x^{(k)}) = \frac{1}{2\pi} \int_{\phi=0}^{2\pi} e^{-in\phi} \delta \hat{V}^{\text{rec}}(x^{(k)}, \phi) d\phi, \quad (48)$$

and

$$\delta \eta^{(n)}(x, r) = \frac{1}{2\pi} \int_{\phi=0}^{2\pi} e^{-in\phi} \delta \eta(x, r, \phi) d\phi. \quad (49)$$

Replacing the latter integrals by finite summations using a trapezoidal integration rule, we arrive at

$$\hat{S}^{(n)}(x, r) = \frac{1}{2\pi} \sum_{m=1}^M e^{-inm\Delta\phi^{(k)}} \hat{S}(x, r, m\Delta\phi^{(k)}) \Delta\phi^{(k)}, \quad (50)$$

$$\delta \hat{V}^{(n); \text{rec}}(x^{(k)}) = \frac{1}{2\pi} \sum_{m=1}^M e^{-inm\Delta\phi^{(k)}} \delta \hat{V}^{\text{rec}}(x^{(k)}, m\Delta\phi^{(k)}) \Delta\phi^{(k)}, \quad (51)$$

and

$$\delta \eta^{(n)}(x, r) = \frac{1}{2\pi} \sum_{m=1}^M e^{-inm\Delta\phi^{(k)}} \delta \eta(x, r, m\Delta\phi^{(k)}) \Delta\phi^{(k)}, \quad (52)$$

where $M\Delta\phi^{(k)} = 2\pi$. After an estimate in the angular Fourier domain for $\delta \eta^{(n)}(x, r)$ for $-N \leq n \leq N$ is obtained, an image of the contrast $\delta \eta(x, r, \phi)$ in

the spatial domain is derived from

$$\delta\eta(x, r, \phi) = \sum_{n=-N}^N \delta\eta^{(n)}(x, r) e^{in\phi}. \tag{53}$$

3.3. Imaging in Bistatic Mode

In order to obtain an estimate for $\delta\eta^{(n)}(\mathbf{v})$ we define the following error functional $F^{(n)}$,

$$F^{(n)} = \sum_{x^{(k)}} \sum_{\omega} \left| \frac{\delta \hat{V}^{(n); \text{rec}}(x^{(k)}, \omega)}{\hat{f}^{\text{trans}}} - \int_{x=-\infty}^{\infty} \int_{r=0}^{\infty} \delta\eta^{(n)}(x, r) \hat{S}^{(n)}((x, r)|(x^{(k)}, r), \omega) r dr dx \right|^2 \Delta x^{(k)} \Delta \omega. \tag{54}$$

Using the following notation in the functional $F^{(n)}$ for $\delta\eta^{(n)}(x, r)$

$$\delta\eta^{(n)}(x, r) = \alpha^{(n)} \Delta\eta^{(n)}(x, r), \tag{55}$$

where $\alpha^{(n)}$ is a real constant and $\Delta\eta^{(n)}(x, r)$ is an update direction, this functional tends to its minimum when $\alpha^{(n)}$ satisfies

$$\alpha^{(n)} = \frac{\Re \left\{ \sum_{x^{(k)}} \sum_{\omega} \frac{\delta \hat{V}^{(n); \text{rec}}(x^{(k)}, \omega)}{\hat{f}^{\text{trans}}} \left[\int_{x=-\infty}^{\infty} \int_{r=0}^{\infty} \Delta\eta^{(n)}(x, r) \hat{S}^{(n)}((x, r)|(x^{(k)}, r), \omega) r dr dx \right]^* \right\}}{\sum_{x^{(k)}} \sum_{\omega} \left| \int_{x=-\infty}^{\infty} \int_{r=0}^{\infty} \Delta\eta^{(n)}(x, r) \hat{S}^{(n)}((x, r)|(x^{(k)}, r), \omega) r dr dx \right|^2}. \tag{56}$$

We interchange the summations and the integrations in the numerator in the right-hand side of this equation. Then we observe that, apart from a constant, this numerator is maximized by taking the update direction to be

$$\Delta\eta^{(n)}(x, r) = \sum_{x^{(k)}} \sum_{\omega} (\hat{S}^{(n)}(x - x^{(k)}, r, \omega))^* \frac{\delta \hat{V}^{(n); \text{rec}}(x^{(k)}, \omega)}{\hat{f}^{\text{trans}}}. \tag{57}$$

Substituting this direction in the numerator of the right-hand side of Eq. (56) we observe that the constant $\alpha^{(n)}$ equals

$$\alpha^{(n)} = \frac{\int_{x=-\infty}^{\infty} \int_{r=0}^{\infty} |\Delta\eta^{(n)}(x, r)|^2 r dr dx}{\sum_{x^{(k)}} \sum_{\omega} \left| \int_{x=-\infty}^{\infty} \int_{r=0}^{\infty} \Delta\eta^{(n)}(x, r) \hat{S}^{(n)}(x - x^{(k)}, r, \omega) r dr dx \right|^2}. \tag{58}$$

Note that $\alpha^{(n)}$ is indeed real and independent of the parameters x , r , and ω . Furthermore, it is noted that the update direction of Eq. (57) represents the back propagation of the data from the data domain to the domain of observation. A summation of the update directions over all angular contributions leads to a first image of the contrast $\delta\eta(\mathbf{v})$ in the subsurface, viz.

$$\delta\eta(\mathbf{v}) = \sum_{n=-N}^N \Delta\eta^{(n)}(x, r). \quad (59)$$

An improved image is obtained when we take into account the minimization constant $\alpha^{(n)}$. In that case $\delta\eta(\mathbf{v})$ is obtained via

$$\delta\eta(\mathbf{v}) = \sum_{n=-N}^N \alpha^{(n)} \Delta\eta^{(n)}(x, r). \quad (60)$$

This back-propagation step yields a first image. For further characterization full inversion is needed [4]. Note that the minimization procedure obtained above is in fact the initial iteration of a conjugate gradient inversion method. By applying such a scheme, further improvements may be achieved, as shown previously for a synthetic example [5]. In the next subsection we present some results based on the two imaging procedures of Eqs. (59) and (60). The former procedure is denoted as the back propagation algorithm, while the latter is denoted as the minimized back propagation algorithm.

3.4. Imaging Results

Both the back propagation and the minimized back propagation algorithms are tested on synthetic and measured data. In both cases “measurements” take place at 64 angular positions.

First we consider a synthetic case, where the homogeneous background medium is characterized by the parameters $\sigma = 0$ and $\epsilon_r = 80$. At a radial distance of two meters in the plane $x = 0$ a point scatterer is positioned with medium parameters $\epsilon_r = 160$ and $\sigma = 1$ S/m. Synthetic data are obtained using Eq. (42). Results from both image processing procedures are given in Figures 10(a) and 10(b). In these figures the computed contrast $\delta\eta(\mathbf{v})$ is shown in the plane $x = 0$. Comparing the results of the two procedures, we observe the expected increase in resolution in the angular direction.

Secondly, we consider a field data set where the data are obtained with the antenna system positioned in a swimming pool. As a scattering object, a metallic gas bottle is positioned in front of the system at a radial distance of two meters. Since the source wavelet and thus the frequency spectrum of the electric current density at the transmitter is unknown, we

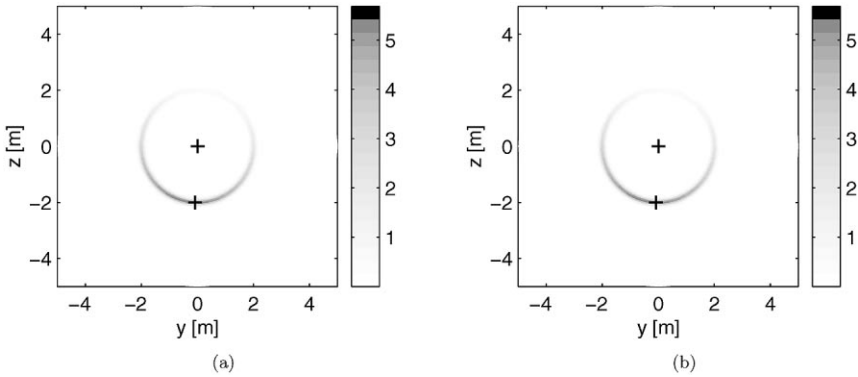


Figure 10. The computed contrast obtained from synthetic data, via (a) back propagation: $\delta\eta^{(n)}(x, r) = \Delta\eta^{(n)}(x, r)$ and (b) minimized back propagation: $\delta\eta^{(n)}(x, r) = \alpha^{(n)}\Delta\eta^{(n)}(x, r)$. The crosses denote the position of the antenna system in the center and the object at a radial distance of two meters.

simply take \hat{I}^{trans} to be equal to one in the image procedure. The measured voltage, contains the signals due to reception of both the direct and the scattered electromagnetic waves. These data are corrected for the direct wave, by subtracting the first trace, $\phi = 0$, from the data set of each trace. The corrected data, shown in Figure 11, are used as input data for both the back propagation and the minimized back propagation algorithm. The image results are shown in Figures 12(a) and 12(b). The figures show the computed contrast for the plane $x = 0$.

Comparing the results of the synthetic and the measured example we observe a similar behavior of the angular dependence of the image distributions.

There are great similarities between the images based on synthetic and measured data, especially in the angular direction. The blurring effect in the radial direction in the image from the measured data is caused through antenna ringing. This effect should be but isn't taken into account in the transmitter current where as source wavelet an impulse function in time is taken. Therefore a deconvolution for the wavelet is omitted and consequently the algorithm will "interpret" the long ringing wavelet as being caused by several reflections from a couple of objects behind each other.

4. Conclusions

In this paper we have discussed the antenna design of a directional borehole radar system. The modeling of the shielded antenna of this radar

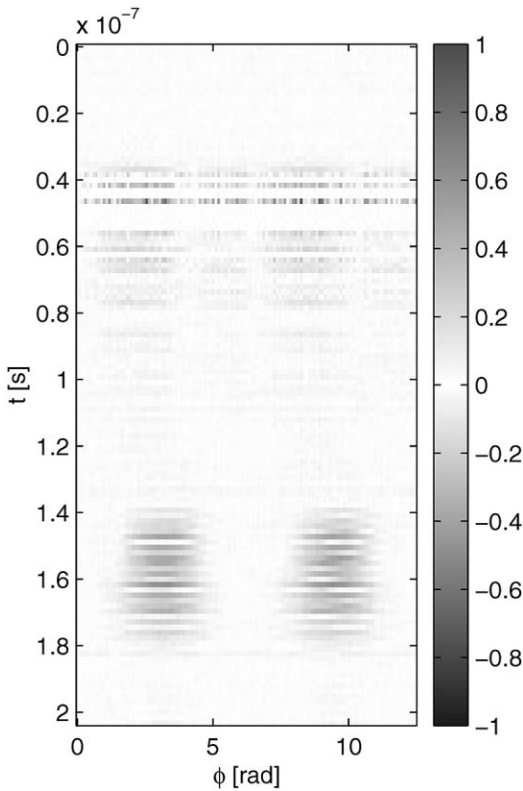


Figure 11. The measured receiver voltage as a function of time and angular position.

system was formulated as an integral equation for the unknown electric surface current density at the surface of the perfectly conducting reflector. This integral equation was numerically solved using an iterative conjugate gradient method; its efficiency was enhanced using a FFT routine for the computation of the convolution in the antenna direction. Based on the modeling results a prototype antenna system was built. The measured radiation pattern was compared with the computed one and they were in close agreement. Furthermore, a simple imaging algorithm based on back propagation has been proposed. Using the computed radiation pattern in this imaging procedure, a deconvolution of the radiation pattern in the angular direction was carried out. Finally we have improved this image procedure by carrying out a minimization procedure where the back propagation is used as an update direction. The result is an increase in angular resolution. We expect improved resolution in radial direction when we take the correct

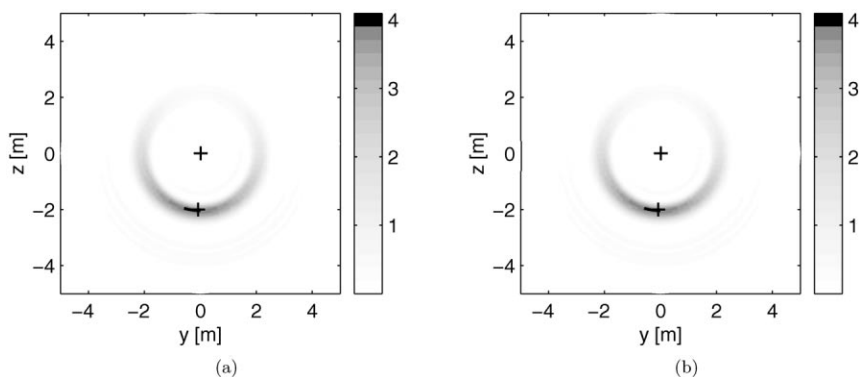


Figure 12. The computed contrast for measured data based on (a) back propagation, $\delta\eta^{(n)}(x, r) = \Delta\eta^{(n)}(x, r)$, and (b) minimized back propagation, $\delta\eta^{(n)}(x, r) = \alpha^{(n)}\Delta\eta^{(n)}(x, r)$. The crosses denote the position of the antenna system in the center and the object at a radial distance of two meters.

source wavelet. In practice a proper estimate of this source wavelet is difficult to obtain.

Acknowledgment

The prototype of the antenna system has been built in cooperation with T&A Radar, Netherlands Organization for Applied Scientific Research (TNO-FEL) and National Aerospace Laboratory (NLR) and partly supported by CODEMA, a committee of the Dutch Ministry of Defense. In particular the authors would like to acknowledge the support of Robert van Ingen and Michiel van Oers, T&A Radar, and Jelle Rodenhuis, TNO-FEL.

References

1. Zwamborn, A.P.M. and Van den Berg, P.M., A weak form of the conjugate gradient FFT method for plate problem: IEEE Transactions on Antennas and Propagation, 1991, v. 39, p. 224–228.
2. Abramowitz, M. and Stegun, I.A., 1970, Handbook of mathematical functions, Dover Publications, New York.
3. De Hoop, A.T., 1995, Handbook of Radiation and Scattering of Waves, Academic Press, London, chapter 28.
4. Van den Berg, P.M., 2002, Scattering and inverse scattering in pure and applied science: Scattering (Pike, R. and Sabatier, P., eds.), v. 2, Academic Press, London, p. 142–161.
5. Van Dongen, K.W.A., Van den Berg, P.M., and Fokkema, J.T., 2001, A directional bore-hole radar: numerical and experimental verification: IEEE AP-S International Symposium and USNC/URSI National Radio Science Meeting, Boston, USA, 8–13 July, Vol. II, ISBN 0 7803 7070 8, p. 746–749.